Experimental validation of a transverse flux magnetic gear

Melaine Desvaux, Marvin Chauwin, Bernard Multon, Stéphane Sire, H. Ben Ahmed

Article Title

Experimental Validation of a Transverse Flux Magnetic Gear

Authors

Melaine Desvaux[1], Marvin Chauwin[1], Bernard Multon[1], Stéphane. Sire[2] and Hamid. Ben Ahmed[1]

Affiliations

1. SATIE Laboratory, ENS Rennes, Université Bretagne Loire, CNRS, 35170 Bruz, France
2. University of Brest, IRDL, CNRS, 29200 Brest, France

Corresponding author(s)

Melaine Desvaux (e-mail: melaine.desvaux@ens-rennes.fr).

Abstract

This article focuses on the realization of a magnetic gear with transverse flux architecture. In order to analyze both the behavior and modeling of this magnetic gear architecture, an experimental test bench was developed, and 3D finite element computations were performed. The instrumentation of this test bench serves to measure torque, transverse flux in pole pieces, speeds and efficiency. A comparison between experimental findings and 3D finite element model output is proposed in order to validate system behavior.

Keywords

Finite element model, instrumentation, magnetic gear, magnetic torque, transverse flux in pole pieces, experimentation.

Article

I. Nomenclature

$B_{av}^{(q)}$: Average transverse flux density in pole piece q [T]
G_m: Gear ratio
N: Number of turns of the sensing coil
p_{LPN}: Number of pole pairs of the low pole number (LPN) ring
p_{HPN}: Number of pole pairs of the high pole number (HPN) ring
q: Pole piece index ($1 < q < Q$)
Q: Number of ferromagnetic pole pieces
S_Q: Pole piece cross-section [m²]
T_{LPN}: Magnetic torque of the low pole number ring [Nm]
T_{HPN}: Magnetic torque of the high pole number ring [Nm]
$U_Q^{(q)}$: Electromotive force generated by flux variation in pole piece q [V]
Ω_{LPN}: Rotational speed of the low pole number ring [rad/s]
Ω_{HPN}: Rotational speed of the high pole number ring [rad/s]
Ω_Q: Rotational speed of the pole piece ring [rad/s]
$\phi_{LPN}^{(q)}$: Total flux in pole piece q from the LPN ring [Wb]
$\phi_{HPN}^{(q)}$: Total flux in pole piece q from the HPN ring [Wb]
φ: Load angle of the magnetic gear [rad]
θ_{HPN}: Angle of the high pole number ring [rad]
θ_{LPN}: Angle of the low pole number ring [rad]

II. Introduction

Many power transmission systems, such as offshore wind turbine drives, include mechanical gearboxes [1-2]. For wind energy harvesting, failure and maintenance of this component cause service interruptions and the need for repairs, which increase strongly operating costs. To improve reliability and availability, replacing these mechanical gearboxes by magnetic gears offers a potentially attractive solution [3-4]. The topology of such a magnetic gear, referred to as a concentric magnetic gear and featuring a high torque density (Fig. 1a), was proposed by Martin [5] and has been the subject of several studies [6-9]. The benefit of a magnetic gear over mechanical gearboxes is more substantial for high-torque applications [10-11].

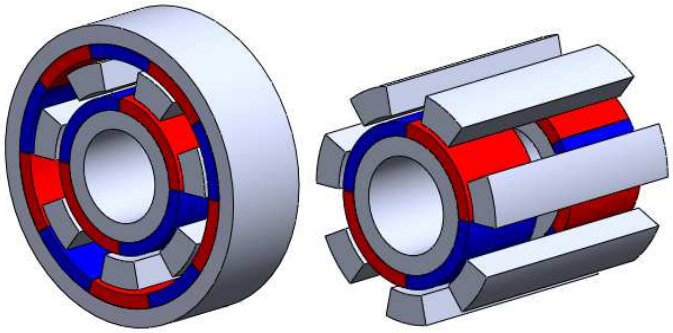

(a) (b)

Fig. 1: Magnetic gear topology, as illustrated by low pole numbers (i.e. p_{LPL} = 2, p_{HPL} = 5, and Q = 7): a) proposed in [6], and b) proposed in [10] and studied in this article

This magnetic gear topology displays apparent weaknesses in terms of mechanical strength. More specifically, the ferromagnetic pole pieces are very elongated structures, laminated perpendicularly to the axis of rotation (in order to minimize iron losses and preserve high system efficiency) and then subjected to magneto-mechanical loads [11]. When considering the position of this ring with pole pieces between two other rings with permanent magnets, it becomes very difficult to increase the stiffness of this ring without degrading the magnetic properties of the magnetic gear.

To increase the stiffness of the pole piece ring and maintain a high torque density, another magnetic gear topology has been proposed in [10] (Fig. 1b). Unlike the concentric topology, this one features an axial flux in the pole pieces, as shown in Fig. 2. This flux is similar to that in the axial magnetic gear [12]; however, the magnetic load remains radial like in [7] (as opposed to the axial magnetic gear [12]), which simplifies the sizing of bearings [13]. Despite the lower torque density when only active part is considered compared to the concentric magnetic gear which weight of the structural part is high as for high-powered wind turbines [14][15][16], the transverse flux magnetic gear seems to be an attractive solution.

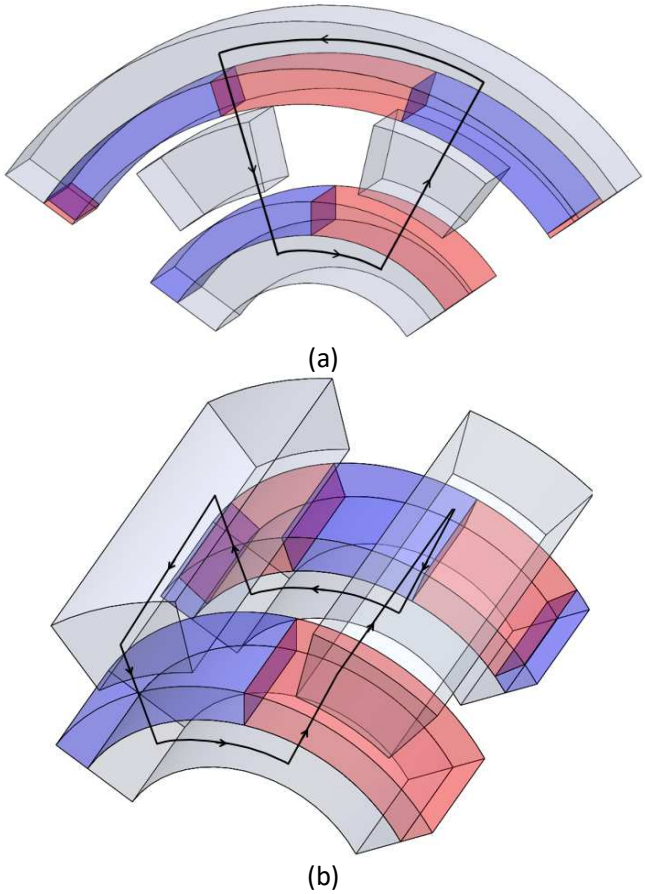

Fig. 2: Flux line paths in magnetic gear topologies: a) concentric magnetic gear without axial flux; and b) with axial flux in pole pieces, proposed in [10].

As is the case for other magnetic gear structures with flux modulation, this topology is

composed of three magnetic parts: a permanent magnet ring with a low pole number (high speed) composed of p_{LPN} pole pairs of permanent magnets and a ferromagnetic yoke; a permanent magnet ring with a high pole number (low speed) composed of p_{HPN} pole pairs of permanent magnets and a ferromagnetic yoke; and an external ring with Q ferromagnetic poles (see Fig. 1 for an example with a low pole number; to facilitate readability: p_{LPN} = 2, p_{HPN} = 5, and Q = 7). To provide magnetic torque, the three ring pole numbers must all respect relation (1). Moreover, to ensure coupling between the two permanent magnet rings, the total flux in pole piece q from the high-speed ring $\phi_{LPN}^{(q)}$ is coupled with the total flux in pole piece q from the high pole number ring $\phi_{HPN}^{(q)}$ (2). Depending on the fixed ring, the gear ratio is given in (3).

$$p_{LPN} + p_{HPN} = Q \tag{1}$$

$$\phi_{LPN}^{(q)} = -\phi_{HPN}^{(q)} \tag{2}$$

$$\begin{cases} \Omega_{LPN} = 0 \rightarrow G_m = \dfrac{\Omega_{HPN}}{\Omega_Q} = \dfrac{Q}{p_{HPL}} \\ \Omega_Q = 0 \rightarrow G_m = \dfrac{\Omega_{LPN}}{\Omega_{HPN}} = -\dfrac{p_{HPL}}{p_{LPL}} \\ \Omega_{HPN} = 0 \rightarrow G_m = \dfrac{\Omega_{LPN}}{\Omega_Q} = \dfrac{Q}{p_{LPL}} \end{cases} \tag{3}$$

Unlike the previous topology, the two permanent magnet rings lie inside the pole piece ring, which more easily increases stiffness of the pole piece ring from the outside, as described in [13-16]. Past studies conducted on this magnetic gear architecture have yielded an understanding of system behavior [13, 16-17]. However, no experimentation has been performed to validate the various magnetic properties, e.g. torque, load angle, transverse flux in pole pieces, and efficiency.

The major contribution of this article consists of the design and creation of a complete experimental bench, including this original magnetic gear architecture [10] and the instrumentation that enables magnetic property evaluation (torque, load angle, transverse flux in pole pieces, efficiency). A comparison with 3D finite element model output serves to validate the magnetic torque of the LPN and HPN rings as well as the transverse flux in pole pieces vs. load angle. Magnetic gear efficiency has also been analyzed for different loads and speeds.

III. Magnetic Gear and Test Bench Creation

A. Magnetic gear design

In order to study the magnetic behavior of this system, one of the three rings needs to be set in a way that allows imposing the gear ratio (3). To derive a simple mechanical design, the preferred solution features stationary pole piece rings. It was also opted to use the magnetic gear as a reducer, with a high-speed motor as input on the LPN rotor, instead of the kind of multiplier found in a wind turbine. The magnetic gear dimensions are listed in Table I, while Figure 3

presents distinct cross-sectional views of the prototype. The dimensions were chosen in order to design as easy as possible a prototype which aims at validating models.

TABLE I
MAGNETIC GEAR DIMENSIONS

Symbol	Quantity	Value
p_{LPN}	Pole pairs in the low pole number ring	4
p_{HPN}	Pole pairs in the high pole number ring	13
Q	Transverse ferromagnetic pole pieces	17
D	External diameter	150 mm
$\delta_{LPN}/\delta_{HPN}$	Radial air gap of the LPN and HPN rings	1.25 mm
e_{PM}	Magnet thicknesses of the LPN and HPN ring	5 mm
e_{yoke}	Yoke thicknesses of the LPN and HPN ring	15 mm
L_z	Magnetic length of the LPN and HPN ring	40 mm
L_Q	Length of the ferromagnetic pole pieces	100 mm
	Thicknesses of pole pieces	22 mm
B_{rem}	Remanence of the NdFeB N30SH magnets	1.105 T
	Permanent magnet splitting of the LPN ring	3
	Permanent magnet splitting of the HPN ring	2
	Ferromagnetic lamination of HPN, LPN and pole pieces ring	0.35 mm
G_m	Gear ratio	3.25

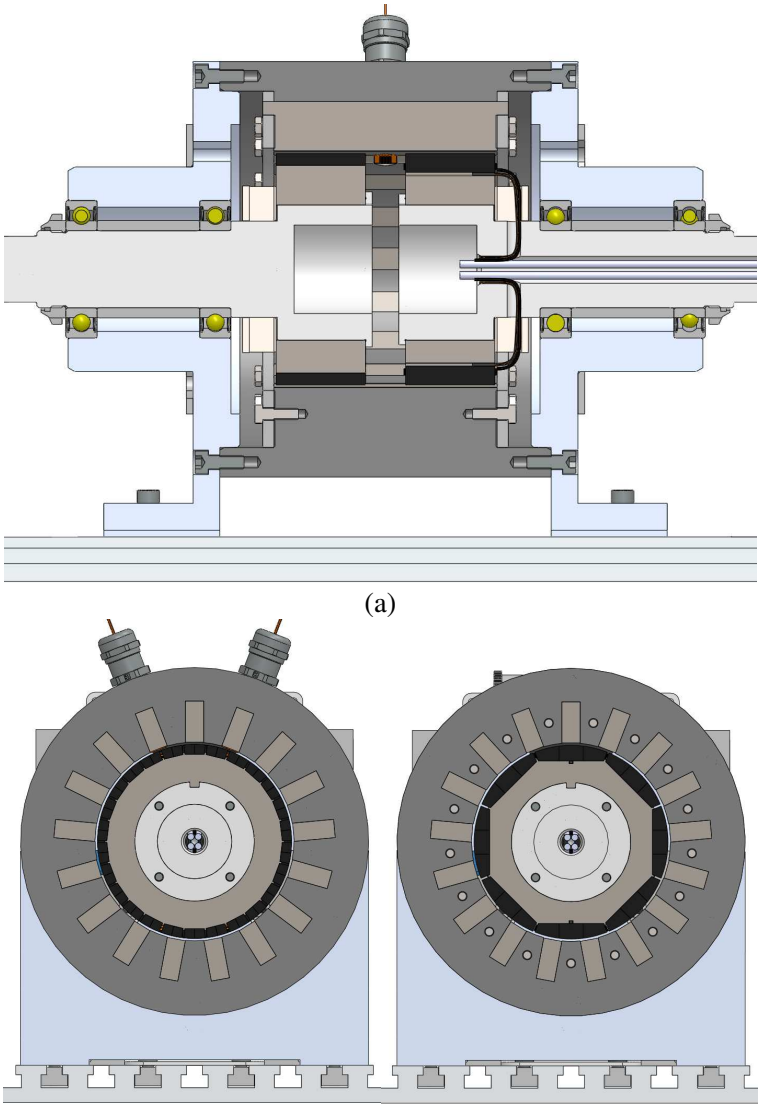

Fig. 3: Cross-sectional views of the magnetic gear prototype described in Table I: a) longitudinal view for observing the mechanical design, b) view of the HPN magnetic plane, and c) view of the LPN magnetic plane

Figures 3b and c indicate that laminated regions (pole pieces and yokes) have a rectangular geometry. Indeed, pole piece lamination necessitates rectangular, rather than radial, pole piece cross-sections. Moreover, permanent magnets are flat on the yoke side and rounded on the airgap side; also, magnetization is parallel. Figure 4 shows the laminated yoke of the LPN ring (Fig. 4a) as well as the positioning of the permanent magnets on the yoke (Fig. 4b).

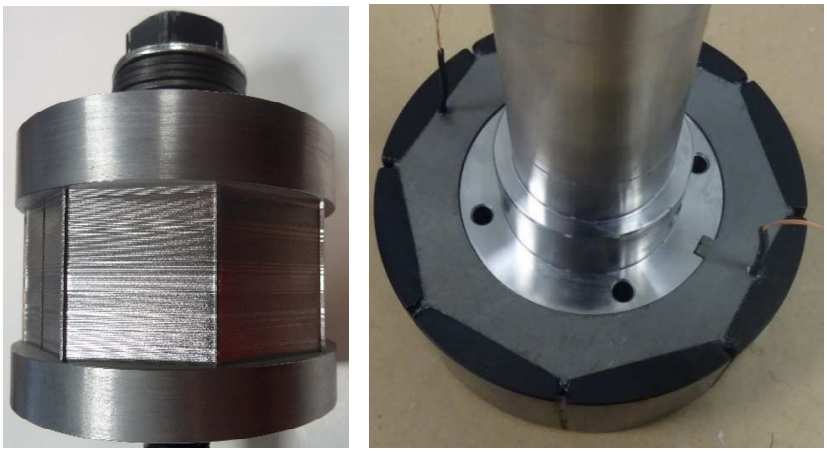

(a) (b)

Fig. 4: Photograph of the LPN ring: a) laminated yoke assembly, and b) permanent magnet positioning on the laminated yoke

B. Test bench

The test bench of the magnetic gear prototype is presented in Figure 5. A permanent magnet 6 Nm-3000 rpm brushless motor is used as the input, controlled by an electronic variator and speed regulated. At the conversion chain output, an air-cooled Magtrol 24 Nm hysteresis brake imposes the resistive torque.

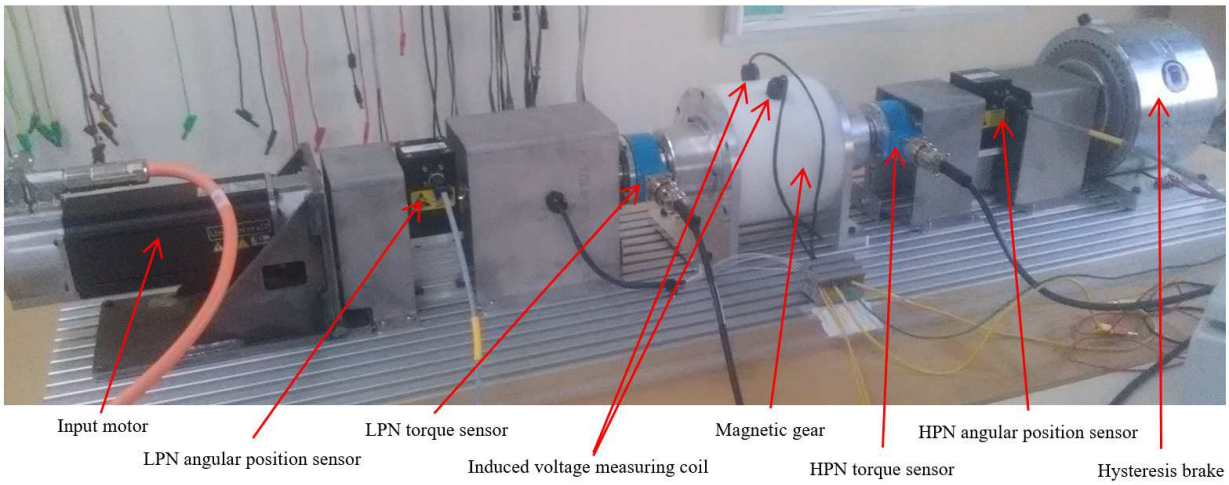

Fig. 5: The test bench set-up

C. Instrumentation

In order to measure torque and efficiency vs. load angle, the test bench contains both angular position sensors and torque sensors placed on either side of the magnetic gear (Fig. 5). The torque sensors used herein are 10 and 20 Nm, 50,000 rpm (Magtrol, resp. TM 307 and TM 308 models), while the incremental encoders are 300 kHz and 3000 rpm with 10-bit resolution (DGS 35).

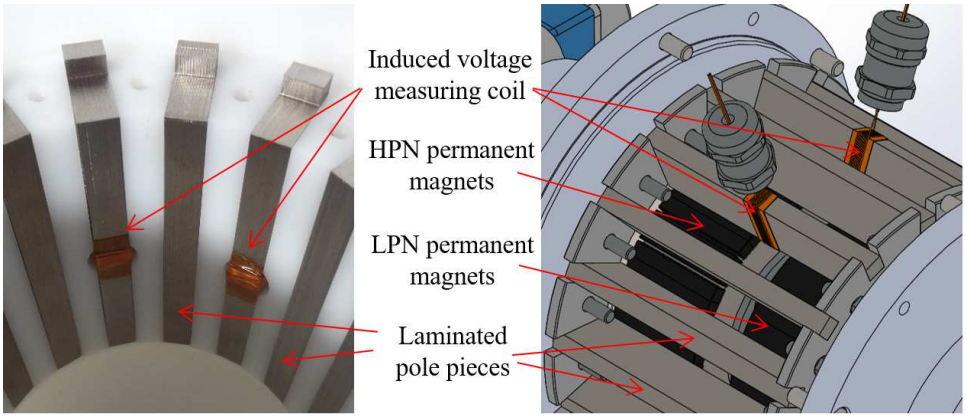

(a) (b)

Fig. 6: Integration of the induced voltage measuring coil generated by the variation of axial flux in pole pieces: a) photograph, and b) numerical view of the integration step

Two phenomena are sought for analysis so as to compare experimental measurements with 3D finite element computations, namely:

- evolution of the average HPN and LPN magnetic torque (T_{HPN} and T_{LPN}) vs. load angle φ (4);
- evolution of the electromotive force generated by the variation in axial flux within pole pieces, which corresponds to the average flux density axial component in a pole piece $B_{av}^{(q)}$, vs. time.

When the pole piece ring is fixed, relation (5) yields the load angle φ. To evaluate this angle, the two angular position sensors are used and their data processed.

To measure the total flux in a pole piece, an electromotive force sensing coil was placed around two pole pieces (shown in Fig. 6). Total flux can be determined by integrating the electromotive force. The relation between average flux density axial component in a pole piece $B_{av}^{(q)}$ and axial flux in a pole piece $\phi_{HPN}^{(q)}$ is given in Equation (6).

$$\begin{cases} T_{HPN} = \widehat{T_{HPN}} \sin(\varphi) \\ T_{LPN} = \widehat{T_{HPN}}.G_m \sin(\varphi) \end{cases} \quad (4)$$

$$\varphi = p_{HPN}.\theta_{HPN} + p_{LPN}.\theta_{LPN} \quad (5)$$

$$B_{av}^{(q)} = \left|\phi_{HPN}^{(q)}/S_Q\right| \quad (6)$$

The measurement of electromotive force $U_Q^{(q)}$ vs. time will be compared with the values calculated using the 3D finite element model. Relation (7) provides the link between electromotive force in a pole piece $U_Q^{(q)}$ and total flux in a pole piece $\phi_{HPN}^{(q)}$, with N being the number of turns in the measuring coil. Insertion of the induced voltage sensing coil into the prototype is shown in Figure 6.

$$U_Q^{(q)} = N\frac{d\,\phi_{HPN}^{(q)}}{dt} = N.\Omega_{HPN}\frac{\Delta\,\phi_{HPN}^{(q)}}{\Delta\,\theta_{HPN}} \quad (7)$$

IV. 3D Finite Element Model

As opposed to modeling the concentric magnetic gear structure [3], it is impossible to carry out the computation using the 2D finite element method [18]. Since induction features an axial component in pole pieces for the transverse flux magnetic gear, a 3D magnetostatic computation is necessary. These experimental results will therefore be compared with the magnetostatic results from the 3D finite element model (3D FEM). The software enabling this study is COMSOL 5.2a [19].

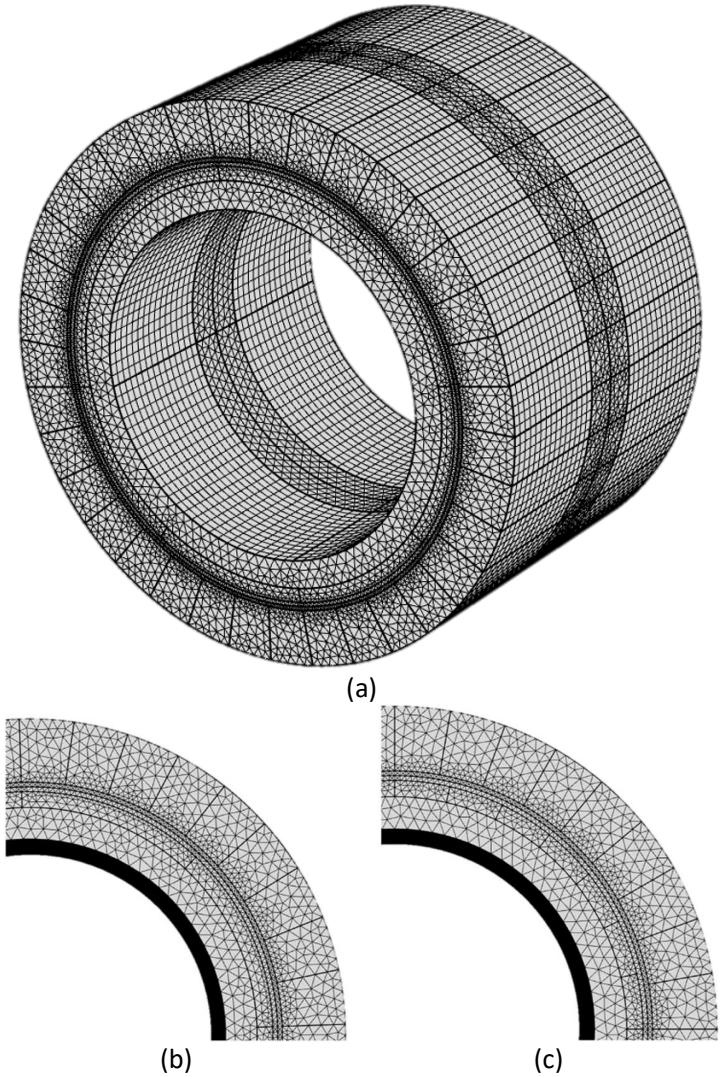

Fig. 7: 3D FEM mesh, produced with COMSOL 5.2a, of the transverse flux magnetic gear with: a) 3D view of the mesh, b) triangular mesh on the LPN ring side, and c) the mesh at the other extremity, i.e. on the HPN ring side

The 3D FEM mesh begins with 5,000 triangles discretizing the sides of both the LPN and HPN planes (see Figs. 7b and c). These triangles are then extruded into a triangular prism in order to obtain approximately 300,000 3D mesh elements (Fig. 7a). The pole piece region, between the two permanent magnet rings and air regions, is meshed with free tetrahedra (Fig. 7a) [20]. The

magnetic field computation is then carried out, resulting in the induction distribution map shown in Figure 8. The computation is performed with external longitudinal air regions not shown in Figure 8. Only those air regions on both sides of the magnet are visible in Figure 8.

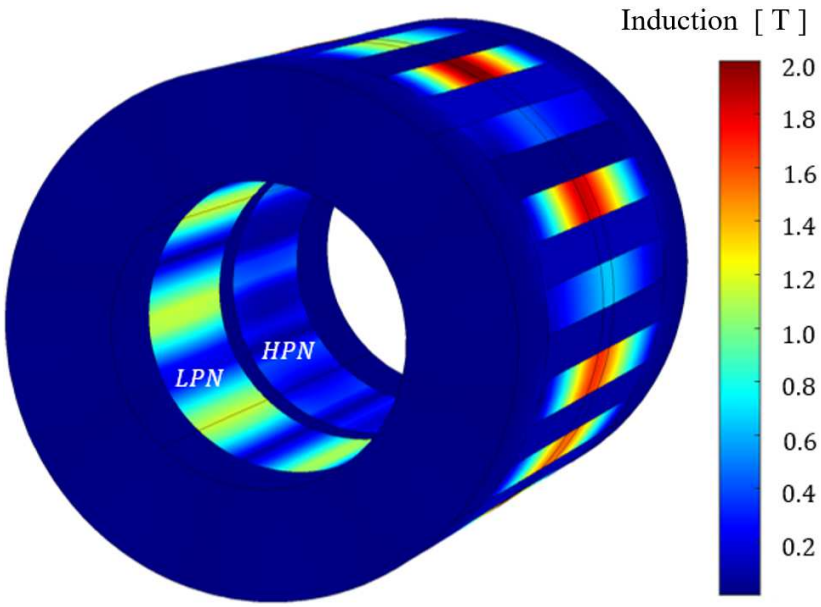

Fig. 8: Induction distribution computed from the 3D finite element method using COMSOL 5.2a

V. Results and Analysis

We have compared various experimental results (electromotive force and torques) with 3D FEM results. Figure 9 shows the evolution in average LPN and HPN torque vs. load angle at 50 rpm for the low-speed rotor (HPN ring). Figure 9 indicates that the 3D finite element model outputs average magnetic torque values very close to the values measured on the prototype (with the maximum error between the 3D FEM computations and experiments equaling 7%). On the other hand, this result enables a torque density on the HPN ring of 141 Nm/m^3 considering permanent magnet volume and 14.9 Nm/m^3 considering active part volume.

With regard to the electromotive force in a pole piece (which represents induction waveforms), Figure 10 displays the comparison of the electromotive force generated by induction variation obtained for different load angles at 50 rpm for the low speed rotor (note that electromotive force has the same evolution pattern at high-speed rotation). Once again, Figure 10 demonstrates that simulations output by the 3D finite element model lie close to experimental measurements.

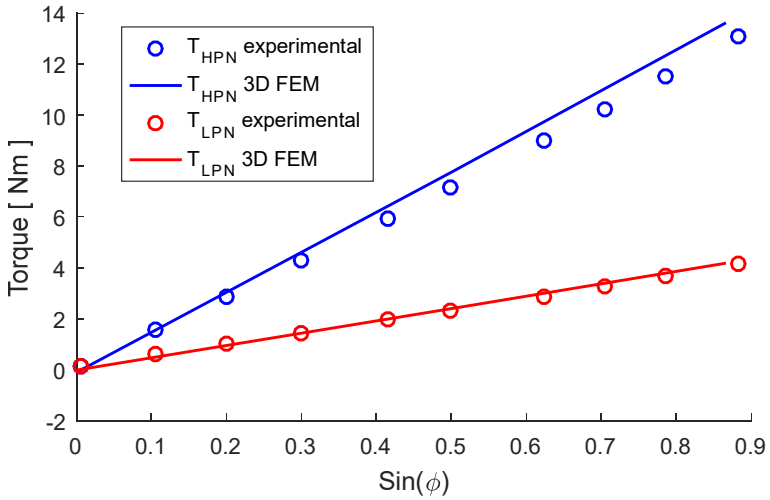

Fig. 9: Average torque evolution vs. load angle obtained from the 3D FEM computation and experimentation on the prototype presented in Table I, at 50 rpm for the low speed rotor

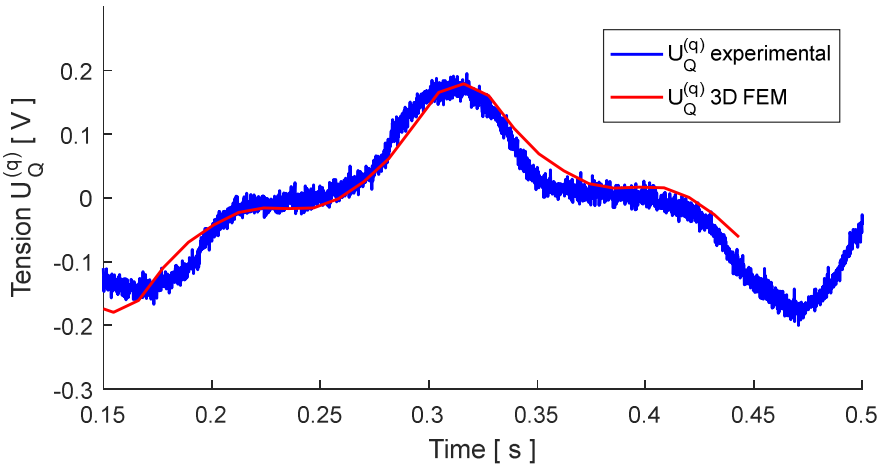

(a)

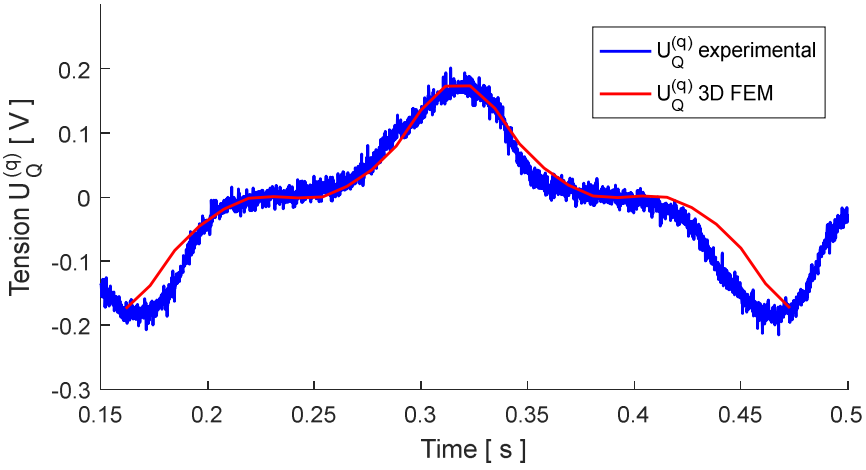

(b)

Fig. 10: Evolution in the electromotive force within a pole piece, as obtained from 3D FEM computations and experimentation for different load angle : a) $\varphi = 30°$, b) $\varphi = 60°$ at 50 rpm for the low speed rotor

The instrumentation developed on the test bench also makes it possible to determine magnetic gear efficiency. Figure 11 thus presents the evolution in efficiency at various speeds vs. load angle. Efficiency is evaluated by holding the load angle constant while increasing the speed of rotation for the range of load angle values. Due to flux modulation (mainly in pole pieces), the magnetic gear exhibits magnetic losses that solely depend on the speed of rotation [21] (Fig. 12 illustrates this phenomenon). A portion of the losses varies in proportion to speed squared, with losses increasing faster than the transmitted power as speed increases [21-22]. By moving at constant speed, losses no longer evolve as evidenced in Figure 12. When load angle increases, efficiency also increases (Fig. 11).

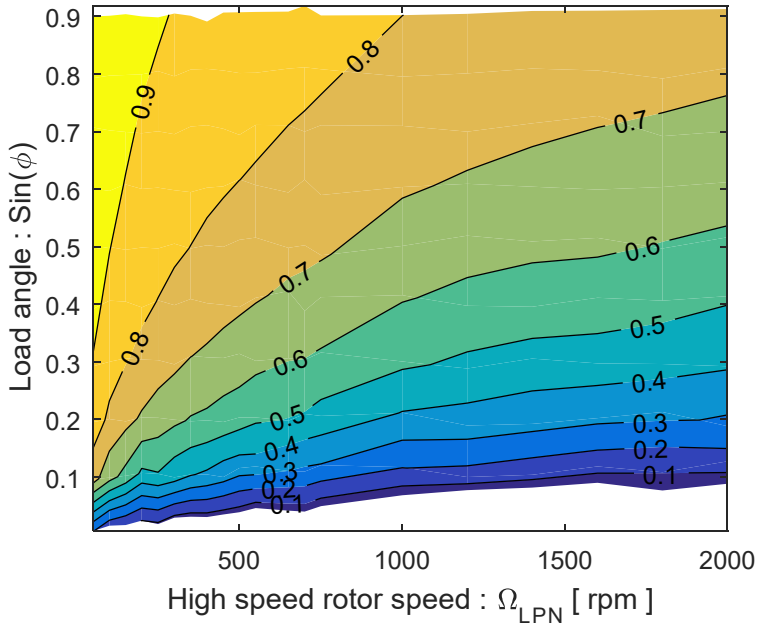

Fig. 11: Efficiency evolution in function of the load angle and LPN speed for the magnetic gear presented in Table I

This evolution in efficiency differs from that of conventional permanent magnet synchronous machines (PMSG). At constant torque, efficiency of PMSG exhibits an optimum with respect to speed [24]. For magnetic gear with transverse flux, the efficiency evolution can be explained by the principle of modulation, which is required for the power transmission with a magnetic gear. Regardless of the load angle value, the magnetic field is strongly rotating (especially in pole pieces), thus induces major losses regardless of the transmitted torque [20, 24].

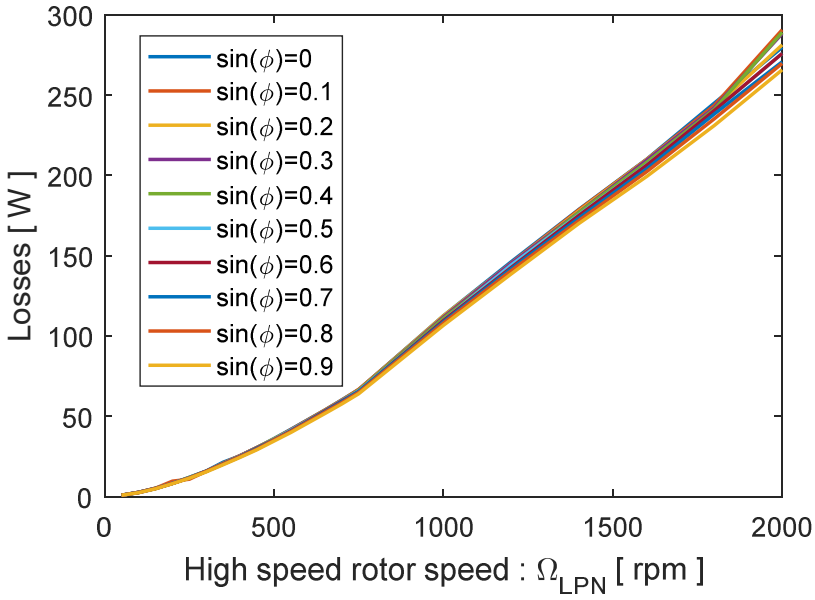

Fig. 12: Losses evolution in function of the load angle and LPN speed for the magnetic gear presented in Table I

VI. Conclusion

This article has presented the design, production and instrumentation of a magnetic gear prototype with a transverse flux, thus enabling comparisons to be drawn between measurements and 3D finite element model simulations. Thanks to the test bench instrumentation, both HPN and LPN torque can be evaluated, along with the electromotive force generated by axial flux variations in pole pieces at different speeds and loads. Results have shown that the 3D finite element model is efficient for purposes of computing these various phenomena. Moreover, an analysis of efficiency derived through experimentation highlights the limitations inherent in applying this transverse flux magnetic gear. The wide variation in pole piece flux generates large iron losses in pole pieces independent of the load. It results significant losses at low load, which constitutes a major disadvantage for many applications.

Acknowledgments

The authors would like to thank ERNEO and Jeumont Electric, with special gratitude being addressed to N. Ziegler, N. Bergeot, D. Laloy, D. Ekeom and A. Fasquelle.

References

[1] J. Keller, Y. Guo, and L. Sethuraman, “Gearbox Reliability Collaborative Investigation of Gearbox Motion and High-Speed-Shaft Loads,” *NREL, Tech. Rep. TP-5000-65321*, 2016.

[2] W. Teng, X. Ding, X. Zhang, Y. Liu, and Z. Ma, “Multi-fault detection and failure analysis of wind turbine

gearbox using complex wavelet transform," *Renew. Energy*, vol. 93, pp. 591–598, 2016, doi: 10.1016/j.renene.2016.03.025.

[3] M. Desvaux, R. Le Goff Latimier, B. Multon, S. Sire, and H. Ben Ahmed, "Analysis of the Dynamic Behaviour of Magnetic Gear with Nonlinear Modelling for Large Wind Turbines," in *2016 XXII International Conference on Electrical Machines (ICEM)*, 2016, pp. 1332–1338.

[4] M. Desvaux, B. Multon, H. Ben Ahmed, S. Sire, A. Fasquelle, and D. Laloy, "Gear Ratio Optimization of a Full Magnetic Indirect Drive Chain for Wind Turbine Applications," *12th Int. Conf. EVER*, 2017.

[5] K. Atallah and D. Howe, "A novel high-performance magnetic gear," *IEEE Trans. Magn.*, vol. 37, no. 4, pp. 2844–2846, 2001, doi: 10.1109/20.951324.

[6] T. B. Martin, "Magnetic transmission," *Pat. US3378710*, 1968, [Online]. Available: https://www.google.com/patents/US3378710?dq=magnetic+transmission&hl=en&sa=X&ei=xCmgU8nYFOSn4gTYvYBA&ved=0CB4Q6AEwAA%5Cnhttp://worldwide.espacenet.com/publicationDetails/biblio?CC=US&NR=3378710A&KC=A&FT=D.

[7] K. Atallah, S. D. Calverley, and D. Howe, "Design, analysis and realisation of a high-performance magnetic gear," *IEE Proc - Electr. Power Appl.*, vol. 151, no. 2, pp. 135–143, 2004, doi: 10.1049/ip-epa:20040224.

[8] E. Gouda, S. Mezani, L. Baghli, and A. Rezzoug, "Comparative study between mechanical and magnetic planetary gears," *IEEE Trans. Magn.*, vol. 47, no. 2, pp. 439–450, 2011, doi: 10.1109/TMAG.2010.2090890.

[9] A. Penzkofer and K. Atallah, "Magnetic Gears for High Torque Applications," *IEEE Trans. Magn.*, vol. 50, no. 11, 2014, doi: 10.1109/TMAG.2014.2328093.

[10] L. Y. L. Yong, X. J. X. Jingwei, P. K. P. Kerong, and L. Y. L. Yongping, "Principle and simulation analysis of a novel structure magnetic gear," *Int. Conf. Electr. Mach. Syst.*, no. 1, pp. 3845–3849, 2008.

[11] M. Desvaux, B. Multon, H. Ben Ahmed, and S. Sire, "Supporting the laminated ferromagnetic pole pieces in a magnetic gear : a structure behaviour analysis from a multibody model," in *6th International Symposium on Multibody Systems and Mechatronics – MuSMe2017*, 2017, pp. 85–94.

[12] S. Mezani, K. Atallah, and D. Howe, "A high-performance axial-field magnetic gear," *J. Appl. Phys.*, vol. 99, no. 8, pp. 97–100, 2006, doi: 10.1063/1.2158966.

[13] SKF, "SKF Rolling Bearings Catalogue," pp. 97–114, 2013.

[14] H. Polinder, D. Bang, R. P. J. O. M. Van Rooij, A. S. McDonald, and M. A. Mueller, "10 MW wind turbine direct-drive generator design with pitch or active speed stall control," 2007, doi: 10.1109/IEMDC.2007.383632.

[15] L. Sethuraman and K. Dykes, "GeneratorSE : A Sizing Tool for Variable-Speed Wind Turbine Generators," *NREL, Tech. Rep. TP-5000-66462*, no. September, 2017, [Online]. Available: www.nrel.gov/publications.

[16] D. Bang, H. Polinder, G. Shrestha, and J. A. Ferreira, "Promising Direct-Drive Generator System for Large Wind Turbines," *2008 Wind Power to Grid - EPE Wind Energy Chapter 1st Semin.*, 2008.

[17] Y. Li, J. W. Xing, Y. P. Lu, and Z. J. Yin, "Torque analysis of a novel non-contact permanent variable transmission," *IEEE Trans. Magn.*, vol. 47, no. 10, pp. 4465–4468, 2011, doi: 10.1109/TMAG.2011.2157807.

[18] W. Bomela, J. Z. Bird, and V. M. Acharya, "The performance of a transverse flux magnetic gear," *IEEE Trans. Magn.*, vol. 50, no. 1, pp. 8–11, 2014, doi: 10.1109/TMAG.2013.2277431.

[19] J. O. Wilkes, *Introduction to COMSOL Multiphysics*. .

[20] M. Desvaux, "Optimisation mécatronique de multiplicateurs magnétiques pour le grand éolien," *PhD Thesis, Ec. Norm. Supérieure Rennes (ENS Rennes)*, 2018.

[21] M. Desvaux, S. Sire, S. Hlioui, B. Multon, and H. Ben Ahmed, "Development of a Hybrid Analytical Model for a Fast Computation of Magnetic Losses and Optimization of Coaxial Magnetic Gears," *IEEE Trans. Energy Convers.*, vol. 34, no. 1, pp. 25–35, 2018.

[22] Y. Zhang, K. Lu, and Y. Ye, "Permanent magnet eddy current loss analysis of a novel motor integrated permanent magnet gear," *IEEE Trans. Magn.*, 2012, doi: 10.1109/TMAG.2012.2200663.

[23] M. Desvaux, B. Multon, S. Sire, and H. Ben Ahmed, "Analytical Iron Loss Model for the Optimization of Magnetic Gear," *IEEE Int. Electr. Mach. Drives Conf. 2017, IEMDC2017*, 2017.

[24] B. Multon, "Conception d'actionneurs spéciaux," *cel-00676242*, 2006.

[25] M. Filippini, P. Alotto, V. Cirimele, and M. Repetto, "Magnetic Loss Analysis in Coaxial Magnetic Gears," *Electronics*, vol. 8, no. 1320, pp. 1–15, 2019, doi: 10.3390/electronics8111320.